Journal of Non-Newtonian Fluid Mechanics 179–180 (2012) 55–68

Contents lists available at SciVerse ScienceDirect

Journal of Non-Newtonian Fluid Mechanics

journal homepage: http://www.elsevier.com/locate/jnnfm

Electro-osmosis of viscoelastic fluids and prediction of electro-elastic flow instabilities in a cross slot using a finite-volume method

A.M. Afonso [a,*], F.T. Pinho [b], M.A. Alves [a]

[a] Departamento de Engenharia Química, Centro de Estudos de Fenómenos de Transporte, Faculdade de Engenharia da Universidade do Porto, Rua Dr. Roberto Frias s/n, 4200-465 Porto, Portugal

[b] Centro de Estudos de Fenómenos de Transporte, Faculdade de Engenharia da Universidade do Porto, Rua Dr. Roberto Frias s/n, 4200-465 Porto, Portugal

ARTICLE INFO

Article history:
Received 18 January 2012
Received in revised form 23 May 2012
Accepted 28 May 2012
Available online 5 June 2012

Keywords:
Electro-osmosis
Viscoelastic fluids
Finite-volume method
Poisson–Nernst–Planck equations
Electro-elastic instabilities

ABSTRACT

This work presents a finite volume method used to solve the relevant coupled equations for general electro-osmotic flows of viscoelastic fluids, using the upper-convected Maxwell and the simplified Phan-Thien–Tanner models.

Three different implementations of the electro-osmosis physical models were carried out, which depend on the required level of approximation. In the first implementation, the Poisson–Nernst–Planck equations were incorporated into the code and the electric charge distribution required to quantify the electric field forcing of the momentum equation is calculated from these fundamental equations. The second implementation is an approximation in which a stable Boltzmann distribution of ions is assumed to occur in the electric double layer, represented by the Poisson–Boltzmann equations. Finally, the so-called Debye–Hückel approximation was also implemented in the Poisson–Boltzmann–Debye–Hückel model, which is valid for cases with a stable Boltzmann distribution of ions characterized by a small ratio of electrical to thermal energies.

Numerical simulations were undertaken in a cross-slot geometry, to investigate the possible appearance of purely electro-elastic flow instabilities, by considering the effect of the electric field. For pure electro-osmotic flow, i.e., in the absence of an imposed pressure gradient, we were able to capture the onset of an unsteady asymmetric flow above a critical Weissenberg number, which is lower than the corresponding value for pressure-driven viscoelastic flow. Additionally, we derive analytically the fully-developed electro-osmosis driven channel flow of polymer solutions described by the FENE-P and PTT models with a Newtonian solvent and assuming a thin electric double layer.

1. Introduction

Accurate flow control in microfluidic devices requires techniques that can easily be miniaturized and an interesting alternative to pressure driven flow control is electrokinetic forcing using electro-osmosis or electrophoresis. An overview of the physical principles of electrokinetic techniques can be found in Bruus [1].

Electro-osmosis (EO) is an electrokinetic phenomenon, first demonstrated by Reuss [2] early in the 19th century, in which the flow of a polar fluid is driven by an external electric field applied between the inlet and outlet of the channel, and acting on ions existing near the channel walls. Helmholtz [3] proposed in 1879 the electric double layer (EDL) theory, which relates the electrical and flow parameters for electrokinetic transport. Subsequently, von Smoluchowski [4] generalized Helmholtz's double layer theory by taking into account the actual charge/potential distributions in a capillary channel. A more realistic concept of these ionic distributions in the fluid adjacent to the capillary wall was introduced by Gouy [5] in 1910 and later by Chapman [6] in 1913. Debye and Hückel [7] determined the ionic number concentration in a solution of low ionic concentration, by means of a linearization of the exponential Boltzmann ion energy distribution.

For Newtonian fluids, rigorous modeling of the electro-osmotic flow (EOF) in microchannels has been the subject of several studies [8–11], and a thorough review on various other aspects of electro-osmosis can be found in Karniadakis et al. [12]. The theoretical study of electro-osmotic flows of non-Newtonian fluids is recent and most works have been restricted to simple inelastic fluid models, such as the power-law, due to the inherent difficulties introduced by more complex constitutive equations [13–16]. Recently these studies were extended to viscoelastic fluids by Afonso et al. [17], who presented analytical solutions for channel and pipe flows of viscoelastic fluids under the mixed influence of electrokinetic and pressure forcings, using two constitutive models: the simplified

* Corresponding author.
E-mail addresses: aafonso@fe.up.pt (A.M. Afonso), fpinho@fe.up.pt (F.T. Pinho), mmalves@fe.up.pt (M.A. Alves).

0377-0257/$ - see front matter © 2012 Elsevier B.V. All rights reserved.
http://dx.doi.org/10.1016/j.jnnfm.2012.05.004

Phan-Thien–Tanner model (sPTT) [18], with linear kernel for the stress coefficient function [19], and the FENE-P model, based on the kinetic theory for Finitely Extensible Non-linear Elastic (FENE) dumbbells with a Peterlin approximation for the average spring force (cf. Bird et al. [20]). The analysis in [17] was restricted to cases with small electric double-layers, where the distance between the walls of a microfluidic device is at least one order of magnitude larger than the EDL, and the fluid had a uniform composition across the channel. Afonso et al. [21] extended this study to the flow of viscoelastic fluids under asymmetric zeta potential forcing and Sousa et al. [22] considered the case in which there is a wall layer depleted of polymer.

In recent years the effort for numerical simulation of EOF has also increased, especially when applied to Newtonian fluids. Yang and Li [23] developed a numerical algorithm for electrokinetically driven Newtonian liquid flows, using the Debye–Hückel approximation [7]. The same approximation was used by Patankar and Hu [24] in the numerical simulation of microfluidic injection of Newtonian fluids, with electro-osmotic forcings through the intersection of two channels. Ermakov et al. [25] developed a finite difference method (FDM) for electro-osmotic and electrophoretic transport and species diffusion for Newtonian fluid flows in two-dimensional complex geometries. Using the Gouy–Chapman approximation [5,6], Bianchi et al. [26] developed a finite-element method (FEM) to study electro-osmotically driven flows of Newtonian fluids in microfluidic T-junctions. Dutta et al. [27] used a spectral element method for the solution of the Poisson–Boltzmann and incompressible Navier–Stokes equations, to analyze mixed electro-osmotic/pressure driven flows of Newtonian fluids in two-dimensional geometries, such as straight channels and T-junction geometries. The work was later extended to complex microgeometries (cross-flow and Y-split junctions) by Dutta et al. [28]. Lin et al. [29] solved the Nernst–Planck and the full Navier–Stokes equations using an FDM to model the EOF of Newtonian fluids in microfluidic flow focusing chips.

For non-Newtonian fluids the efforts for numerical modeling of EOF are now gathering momentum, with limited advances having been made, still for very simple geometries such as straight microchannels. Recently, Park and Lee [30] calculated numerically the electro-osmotic velocity of viscoelastic fluids in a square microchannel with and without externally imposed pressure gradient, using a generalized constitutive equation, which encompasses the upper-convected Maxwell (UCM), the Oldroyd-B and the PTT models. Tang et al. [31], presented a numerical study of EOF in microchannels of generalized Newtonian fluids (GNFs) described by the power law model, using the lattice Boltzmann method. More recently, Tang et al. [32] used the lattice Boltzmann method to simulate the pressure-driven and electro-osmotic flows of non-Newtonian fluids in porous media, using the Herschel–Bulkley model for rheological characterization of the non-Newtonian fluid. Based on the representative elementary volume scale to represent the porous medium, the results obtained for the velocity profiles agreed well with analytical solutions. Zimmerman et al. [33] presented two-dimensional FEM simulations of EOF in a microfluidic T-junction of GNFs described by a Carreau-type nonlinear viscosity function. The motion within the electrical double layer at the channel walls was approximated using velocity wall slip boundary conditions. Electrokinetic forcing can lead to the onset of flow instabilities, called electrokinetic instabilities. When combined with viscoelastic fluids, new instability phenomena arise, as recently discovered by Bryce and Freeman [34]. However, a sound understanding of the driving mechanism of these electro-elastic instabilities is still missing.

In this work, numerical simulations of EOF of viscoelastic fluids in complex geometries are reported for the first time, to our best knowledge. We use a FVM to solve the relevant coupled equations for electro-osmotic flows of viscoelastic fluids, namely the nonlinear Poisson–Nernst–Planck equation that governs the electrical double-layer field, the momentum equation with a body force due to the applied electrical potential field and two constitutive equations for the viscoelastic fluids, namely the UCM and sPTT models. In addition to the simulations in a complex geometry (cross-slot geometry), and in order to test the implementation of the numerical method, some predictions are compared with analytical solutions for the flow in a two-dimensional microchannel under symmetric and asymmetric zeta potentials at the walls [17,21].

The remaining of the paper is organized as follows: in Sections 2 and 3 we briefly present the governing equations and outline the numerical method used to simulate the EOF of the viscoelastic fluids, respectively. In Sections 4.1 and 4.2, the main results of the verification of the numerical method and of the EOF in a cross-slot geometry are presented, respectively. A summary of the main findings closes the paper in section 5. Additionally, in Appendix A we present the analytical solution of PTT and FENE-P fluids with a Newtonian solvent contribution for fully-developed flow in a straight channel.

2. Governing equations

The flow is assumed to be laminar and the fluid is incompressible. The governing equations describing the flow of the viscoelastic polymer solution are the continuity equation,

$$\nabla \cdot \mathbf{u} = 0 \tag{1}$$

and the momentum equation:

$$\rho\left[\frac{\partial \mathbf{u}}{\partial t} + \nabla \cdot \mathbf{uu}\right] = -\nabla p + \beta\eta_0\nabla^2\mathbf{u} + \frac{\eta_0}{\lambda}(1-\beta)\nabla \cdot \mathbf{A} + \mathbf{F} \tag{2}$$

where $\mathbf{u}$ is the velocity vector, p the pressure, t the time, ρ the fluid density, η_s the constant solvent viscosity and $\mathbf{A}$ is the polymer conformation tensor. The total fluid extra stress is the sum of the solvent and polymer stress contributions, where the latter is described by the sPTT model, which includes the particular case of the UCM model. The polymer has a relaxation time λ and a viscosity coefficient η_p, defining a zero-shear rate total viscosity $\eta_0 = \eta_p + \eta_s$. The coefficient β in Eq. (2) is the ratio between the solvent viscosity and η_0 ($\beta = \eta_s/\eta_0$). When $\beta = 0$ there is no solvent contribution and $\beta = 1$ corresponds to a Newtonian fluid, i.e., there is no polymer additive. When $\beta < 1$ (which implies $\lambda > 0$ for the polymeric contribution), the polymer extra-stress tensor $\boldsymbol{\tau}$ can be related to the conformation tensor $\mathbf{A}$ using

$$\boldsymbol{\tau} = \frac{\eta_p}{\lambda}(\mathbf{A} - \mathbf{I}) \tag{3}$$

which requires the solution of an evolution equation for $\mathbf{A}$ of the form,

$$\lambda\left[\frac{\partial \mathbf{A}}{\partial t} + \nabla \cdot \mathbf{uA}\right] + Y(\mathrm{tr}\mathbf{A})\mathbf{A} = Y(\mathrm{tr}\mathbf{A})\mathbf{I} + \lambda(\mathbf{A}\cdot\nabla\mathbf{u} + \nabla\mathbf{u}^T\cdot\mathbf{A}) \tag{4}$$

where $\mathbf{I}$ is the unitary tensor. In its general form function $Y(\mathrm{tr}\mathbf{A})$ is exponential, but in this work we use the linear form [19,20]

$$Y(\mathrm{tr}\mathbf{A}) = 1 + \varepsilon(\mathrm{tr}\mathbf{A} - 3) \tag{5}$$

When $Y(\mathrm{tr}\mathbf{A}) = 1$ the Oldroyd-B model is recovered which further simplifies to the UCM equation if additionally $\beta = 0$. In the general case ($\varepsilon \neq 0$ and $\beta \neq 0$), Eqs. (4) and (5) describe the sPTT model with a Newtonian solvent. The function $Y(\mathrm{tr}\mathbf{A})$ imparts shear-thinning behavior to the fluid and bounds the extensional viscosity as explained in the original papers of Phan-Thien and Tanner [18] and Phan-Thien [19].

In the log-conformation tensor approach adopted in the numeric solution of Eq. (4), the transformation $\boldsymbol{\Theta} = \log\mathbf{A}$ is applied

to Eq. (4) as described by Fattal and Kupferman [35], leading to the following evolution equation in $\boldsymbol{\Theta}$:

$$\frac{\partial \boldsymbol{\Theta}}{\partial t} + (\mathbf{u}\cdot\nabla)\boldsymbol{\Theta} - (\mathbf{R}\boldsymbol{\Theta} - \boldsymbol{\Theta}\mathbf{R}) - 2\mathbf{B} = \frac{Y[\mathrm{tr}(e^{\boldsymbol{\Theta}})]}{\lambda}(e^{-\boldsymbol{\Theta}} - \mathbf{I}). \tag{6}$$

The tensors $\mathbf{B}$ and $\mathbf{R}$ are the traceless extensional and pure rotational components of the velocity gradient, $\nabla\mathbf{u}$, respectively. To recover $\mathbf{A}$ from $\boldsymbol{\Theta}$ the inverse transformation $\mathbf{A} = e^{\boldsymbol{\Theta}}$ is used. The log-conformation approach [35] is a relevant particular case of the recently proposed kernel-conformation tensor transformation [36], in which several matrix transformations can be applied to the evolution equation of the conformation tensor. The log-conformation tensor approach introduces a better polynomial interpolation of the stresses when these exhibit an exponential growth, such as near stagnation points, with the added advantage of preserving the positive definiteness of the conformation tensor. These features have been extensively explained elsewhere [35,36].

The $\mathbf{F}$ term in the momentum Eq. (2) represents the electric body force per unit volume, given as

$$\mathbf{F} = \rho_e \mathbf{E} \tag{7}$$

where $\mathbf{E}$ is the applied external electric field and ρ_e is the net electric charge density in the fluid. The electric field is related to the electric potential, Φ, by

$$\mathbf{E} = -\nabla\Phi \tag{8}$$

while the electric potential is governed by,

$$\nabla^2\Phi = -\frac{\rho_e}{\epsilon} \tag{9}$$

where ϵ is the electrical permittivity of the solution, given by the product of the dimensionless dielectric constant of the solution and the vacuum permittivity. Two electric fields are relevant in EOF flows: one is the applied electric field, ϕ, generated by the electrodes at the inlet and outlet of the flow geometry; the other electric field is due to the net charge distribution in the EDL, ψ, associated to the charge acquired by the fluid near the walls. The total electric field is given by a linear superposition of these two contributions,

$$\Phi = \phi + \psi \tag{10}$$

Eqs. (9) and (10) can be rewritten as two separate equations,

$$\nabla^2\phi = 0 \tag{11}$$

and

$$\nabla^2\psi = -\frac{\rho_e}{\epsilon}. \tag{12}$$

Finally, the electric charge density needs to be quantified in order to generate a closed-form system of equations. For a symmetric electrolyte the ions and the counter-ions have the same charge valence, $z^+ = -z^- = z$, and the net electric charge density is given by:

$$\rho_e = ez(n^+ - n^-), \tag{13}$$

where n^+ and n^- are the concentrations of the positive and negative ions, respectively, and e is the elementary electric charge. In order to find the net charge density ρ_e, the distributions of ionic concentrations n^+ and n^- must be determined. This is achieved by solving the following convection–diffusion equation for the ion concentrations, known as the Nernst–Planck equation:

$$\frac{\partial n^\pm}{\partial t} + \mathbf{u}\cdot\nabla n^\pm = \nabla\cdot(D^\pm\nabla n^\pm) \pm \nabla\cdot\left[D^\pm n^\pm \frac{ez}{k_BT}\nabla(\phi+\psi)\right] \tag{14}$$

where D^+ and D^- are the diffusion coefficients of the positive and negative ions, respectively. The set of Eqs. (11)–(14) is usually called the Poisson–Nernst–Planck equations (PNP).

Another way to quantify the electric charge density is using the widely adopted Poisson–Boltzmann equation derived from the Nernst–Planck equations. In many circumstances, when the flow (and the ionic distribution) is stationary, the electric double layer does not overlap at the center of the channel and significant variations of $n^\pm$ and ψ occur only in the normal direction to the channel walls, in which case the stable Boltzmann distribution of ions in the electric double layer can be assumed, leading to [1]:

$$\frac{n^\pm}{n_o} = \exp\left(\mp\frac{ez}{k_BT}\psi\right) \tag{15}$$

Combining Eqs. (13) and (15), leads to the following electric charge density distribution:

$$\rho_e = -2n_o ez\sinh\left(\frac{ez}{k_BT}\psi\right) \tag{16}$$

where $n_o = CN_A$ is the bulk number concentration of ions in the electrolyte solution, C is the molar concentration of ions, N_A is Avogadro's number, T is the absolute temperature and k_B is the Boltzmann constant. The set of Eqs. (11), (12) and (16) is usually called the Poisson- Boltzmann equations (PB).

For small values of $ez\psi_0/k_BT$, synonymous of a small ratio of electrical to thermal energies, Eq. (16) can also be linearized, since $\sinh x \approx x$ (ψ_0 is the maximum value of ψ, at the wall). This is the so-called Debye–Hückel approximation for which the electric charge density equation becomes

$$\rho_e = -\epsilon\kappa^2\psi \tag{17}$$

where $\kappa^2 = \frac{2n_oe^2z^2}{\epsilon k_BT}$ is the Debye–Hückel parameter, related to the thickness of the Debye layer, (also referred to as the EDL thickness, $\lambda_D = \kappa^{-1}$). The set of Eqs. (11), (12) and (17) is usually called the Poisson–Boltzmann–Debye–Hückel equations (PBDH).

Finally, we can rewrite the momentum Eq. (2) as,

$$\frac{D\mathbf{u}}{Dt} = -\nabla p + \beta\eta_0\nabla^2\mathbf{u} + \frac{\eta_0}{\lambda}(1-\beta)\nabla\cdot\mathbf{A} - \rho_e\nabla(\phi+\psi) \tag{18}$$

keeping in mind that the electric charge density can be obtained from Eqs. (13), (16) or (17), depending on the required level of approximation.

It is appropriate at this point to make some considerations regarding the validity of the various electrokinetic models. The relevant time-scales in the momentum and constitutive equations are the convection time-scale, $t_{conv} = H/U$, the momentum diffusion time-scale, $t_{diff-mom} = \rho H^2/\eta$, and the fluid (relaxation) time-scale, $t_{fluid} = \lambda$. In our computations we keep the Reynolds number very small ($Re = t_{diff-mom}/t_{conv} \ll 1$), thus we can neglect the momentum diffusion time-scale, $t_{diff-mom} \ll t_{conv}$, which is equivalent to neglecting the convection term in the momentum equation. When the Nernst–Planck equation is used, the time scale of the diffusion transport of the ions, $t_{diff-ions} = 1/(\kappa^2 D)$, becomes also relevant. The Nernst–Planck model will lead to similar results as the approximate Poisson–Boltzmann model when this time-scale is significantly lower than the convection time scale and fluid relaxation time. These can be written as $\frac{t_{diff-ions}}{t_{conv}} < 1$ and $\frac{t_{diff-ions}}{t_{fluid}} < 1$, which leads to the following criteria for accurate use of the Poisson–Boltzmann equation (notice that here $U \approx u_{sh}$) : $Pe = \frac{UH}{D} < \bar{\kappa}^2$ and $\frac{Pe}{Wi_H} < \bar{\kappa}^2$. These conditions are easily satisfied with thin EDL.

3. Numerical method

The finite-volume method used is based on a time marching pressure-correction algorithm formulated with the collocated variable arrangement, as explained in detail in Oliveira et al. [37] and Alves et al. [38]. For improved convergence, the FVM was modified

with the matrix logarithm of the conformation tensor [35], and details of that implementation were reported by Afonso et al. [39].

In this work, the existing numerical method [39] was generalized to simulate mixed electro-osmotic/pressure driven flows, and the required modifications are explained below. We note that the equations for the pressure and extra stress components (or the log-conformation tensor) are the same used in the pressure-driven flow version of the code (see [37,38]), and so they are not described in detail here. The Coulombic force term in the momentum Eq. (2) is introduced directly to the source term and no significant modifications are necessary, including the SIMPLEC pressure correction algorithm.

As described in the previous section, the new set of equations depends on the approximations applied to the closed-form equation for the electric charge density, i.e., the PNP, PB or PBDH equations. This fact also reflects on the numerical implementation, and we chose to implement all the three approximations and compare them. Briefly, the PNP, PB or PBDH equations are transformed first to a non-orthogonal coordinate system, but keeping the Cartesian velocity and stress components in Cartesian coordinates [37]. Then, the equations are integrated in space over the control volumes (cells with volume V_P) forming the computational mesh, and in time over a time step (δt), so that sets of linearized algebraic equations are obtained, having the general form:

$$a_P^\theta \theta_P = \sum_{F=1}^{6} a_F^\theta \theta_F + S^\theta \tag{19}$$

to be solved for the variables ($\theta = u, v, w, p, \tau_{ij}, \phi, \psi, n^+$ and n^-). In these equations a_F are coefficients accounting for convection and diffusion, S^θ are source terms encompassing all contributions not included in the coefficients, the subscript P denotes the cell under consideration and subscript F denotes its corresponding neighboring cells.

For the PNP model, the coefficients of the discretized equations are given by:

$$\text{For the } \phi \text{ equation} \Rightarrow \left\{ a_F^\phi = D_f; \quad a_P^\phi = \sum_{F=1}^{6} a_F^\phi; \quad S^\phi = 0 \right. \tag{20}$$

$$\text{For the } \psi \text{ equation} \Rightarrow \left\{ a_F^\psi = D_f; \quad a_P^\psi = \sum_{F=1}^{6} a_F^\psi; \quad S^\psi = \frac{ez}{\epsilon}\left(n_P^+ - n_P^-\right) V_P \right. \tag{21}$$

For the Nernst–Planck equations, the following coefficients of the algebraic discretized equations are used to determine $n^\pm$,

$$n^\pm \Rightarrow \begin{cases} a_F^{n^\pm} = D_f + C_f; a_P^{n^\pm} = \frac{V_P}{\delta t} + \sum_{F=1}^{6} a_F^{n^\pm} \\ S^{n^\pm} = S_{HRS}^{n^\pm} + \frac{V_P n_P^{\pm 0}}{\delta t} \pm \sum_{f=1}^{6} \left(\sum_{l=1}^{3} B_{fl}^f g_{lf} \right) \end{cases} \tag{22}$$

where g_l is the l component of $\boldsymbol{g} = D^\pm n^\pm \frac{ze}{k_b T} \nabla(\phi + \psi)$. For the momentum equation, the coefficients a_P and a_F are unchanged (cf. [37,38]) and the additional source term associated with the Coulombic force is given by

$$u, v, w \Rightarrow \left\{ S_E^{uvw} = ez\left(n_P^- - n_P^+\right) \sum_{l=1}^{3} B_l^P [\Delta(\phi_P + \psi_P)]_l^P V_P \right. \tag{23}$$

This new additive source term S_E^{uvw} represents the electric body force term in the momentum Eq. (2) and is added to the other source terms used in the pressure-driven version of the code (see [37,38]). In Eqs. (20)–(23), D_f and C_f are the diffusive and convective conductances, respectively, B_l^P represents the area components of the surface along direction l and $[\Delta\theta]_l^P$ are the differences between values of θ along direction l (cf. [37] for details and mathematical definitions). The CUBISTA high-resolution scheme [38] was used to discretize the convective terms of the ionic transport Eq. (14), together with the deferred correction approach. This implies that the convective conductance C_f is based on the upwind differencing scheme (UDS) and the term $S_{HRS}^{n^\pm}$ introduced in Eq. (21) represents the difference between the CUBISTA high-resolution scheme fluxes and the UDS fluxes, here evaluated explicitly based on the previous time level. The CUBISTA scheme is formally of third-order accuracy and was especially designed for differential rheological constitutive relations [38].

For the PB model of electro-osmosis, the coefficients of the discretized governing equations are given by:

$$\begin{aligned} \phi &\Rightarrow \left\{ a_F^\phi = D_f; \quad a_P^\phi = \sum_{F=1}^{6} a_F^\phi; \quad S^\phi = 0 \right. \\ \psi &\Rightarrow \left\{ \begin{array}{l} a_F^\psi = D_f; \quad a_P^\psi = \sum_{F=1}^{6} a_F^\psi + \kappa^2 \cosh\left(\frac{ez}{k_B T}\psi_P\right) V_P \\ S^\psi = \left[\kappa^2 \psi_P \cosh\left(\frac{ez}{k_B T}\psi_P\right) - 2\frac{n_o ez}{\epsilon} \sinh\left(\frac{ez}{k_B T}\psi_P\right)\right] V_P \end{array} \right. \end{aligned} \tag{24}$$

The non-linear hyperbolic function $\sinh(ez\psi/k_BT)$ poses a challenge in the numerical solution of the PB equation, due to the associated exponential nonlinearity. Here, in order to prevent the numerical divergence due to this exponential nonlinearity near the walls, the special treatment of the source term S^ψ proposed by Dutta et al. [28] is used, with the inclusion on both sides of the equation of terms containing $\cosh(ez\psi/k_BT)$ into the S^ψ and a_P^ψ terms, for enhanced stability. The additional source term of the momentum equation, associated with Coulombic force is now given by

$$u, v, w \Rightarrow \left\{ S_E^{uvw} = 2 n_o ez \sinh\left(\frac{ez}{k_B T}\psi_P\right) \sum_{l=1}^{3} B_l^P [\Delta(\phi_P + \psi_P)]_l^P V_P \right. \tag{25}$$

Finally, for the PBDH model of electro-osmosis, the coefficients of the discretized equations are given by:

$$\begin{aligned} \phi &\Rightarrow \left\{ a_F^\phi = D_f; \quad a_P^\phi = \sum_{F=1}^{6} a_F^\phi; \quad S^\phi = 0 \right. \\ \psi &\Rightarrow \left\{ a_F^\psi = D_f; \quad a_P^\psi = \sum_{F=1}^{6} a_F^\psi + \kappa^2 V_P; \quad S^\psi = 0 \right. \end{aligned} \tag{26}$$

and the additional source term of the momentum equation is now given by

$$u, v, w \Rightarrow \left\{ S_E^{uvw} = \epsilon \kappa^2 \psi_P \sum_{l=1}^{3} B_l^P [\Delta(\phi_P + \psi_P)]_l^P V_P \right. \tag{27}$$

4. Results and discussion

4.1. Code verification

To test the implementation of the numerical method some predictions are compared with existing analytical solutions for the flow of a PTT fluid in a two-dimensional microchannel under symmetric and asymmetric boundary conditions for the zeta potential at the walls [17,21]. The comparison with the analytical solution for the pure electro-osmotic flow of a PTT model with a solvent viscosity contribution ($\beta \neq 0$) is also used. This analytical solution is presented in detail in Appendix A.

In all these cases, the so-called standard electrokinetic model assumptions were used, along with the sPTT model for the viscoelastic fluid. When the flow is fully-developed the velocity and

stress fields only depend on the transverse coordinate y, on ϵ, E_x and ζ_i via the Helmholtz–Smoluchowski electro-osmotic velocity $u_{sh} = -\epsilon\zeta_1 E_x/\eta$, and on some dimensionless quantities, such as the ratio of microchannel to Debye layer thicknesses $\bar{\kappa} = \kappa H$, on the rheological properties of the fluid via a Weissenberg number based on the EDL thickness and u_{sh}, $Wi_\kappa = \lambda u_{sh}/\lambda_D = \lambda u_{sh}\kappa$ (or based in the channel thickness, $Wi_H = \lambda u_{sh}/H$ as in [17]) and the fluid extensibility parameter ε. Additionally, to quantify the combined pressure gradient and electro-osmosis forcings, the non-dimensional ratio between these two forcings is given by $\Gamma = -(H^2/\epsilon\zeta_1)(p_{,x}/E_x)$, where $p_{,x}$ is the pressure gradient.

The channel geometry is represented in Fig. 1a. At the walls the no-slip condition applies ($u = 0$ at $y = \pm H$), along with $\partial\phi/\partial y_{|wall} = 0, \psi = \zeta_i$ and $n^{\pm} = n_o \exp\left(\mp \frac{ez}{k_B T}\zeta_i\right)$. Depending on the value of the zeta potential at the walls, ζ_i , we can determine if the flow is symmetric ($R_\zeta = \zeta_1/\zeta_2 = 1$, i.e. $\zeta_1 = \zeta_2$) or asymmetric ($R_\zeta = \zeta_1/\zeta_2 \neq 1$, i.e. $\zeta_1 \neq \zeta_2$). At the inlet fully-developed velocity and stress profiles are imposed and at the outlet planes Neumann boundary conditions are applied, i.e. $\partial/\partial x = 0$ for all quantities (all θ), except for pressure which is linearly extrapolated at the outlet from the two upstream cells.

The main characteristics of the three meshes used in this work for the accuracy test are given in Table 1, including the total number of cells (NC) and the minimum cell spacing ($\Delta x_{min}/H$ and $\Delta y_{min}/H$). Note that the refinement in the transverse direction is very high, in order to obtain accurate results in the EDL where sharp gradients are observed. This high refinement is shown in Fig. 1b, here for mesh M_3.

The results for the accuracy tests are presented in Figs. 2 and 3. Fig. 2 compares the velocity profiles obtained with the numerical simulations using the PB formulation and those obtained from the corresponding analytical solutions [17,21]. When $R_\zeta = 1$, i.e., for symmetric conditions, Fig. 2a, shows the fully-developed dimensionless velocity profiles obtained with $\varepsilon = 0.25$, $\beta = 0$, $Wi_\kappa = 1$,

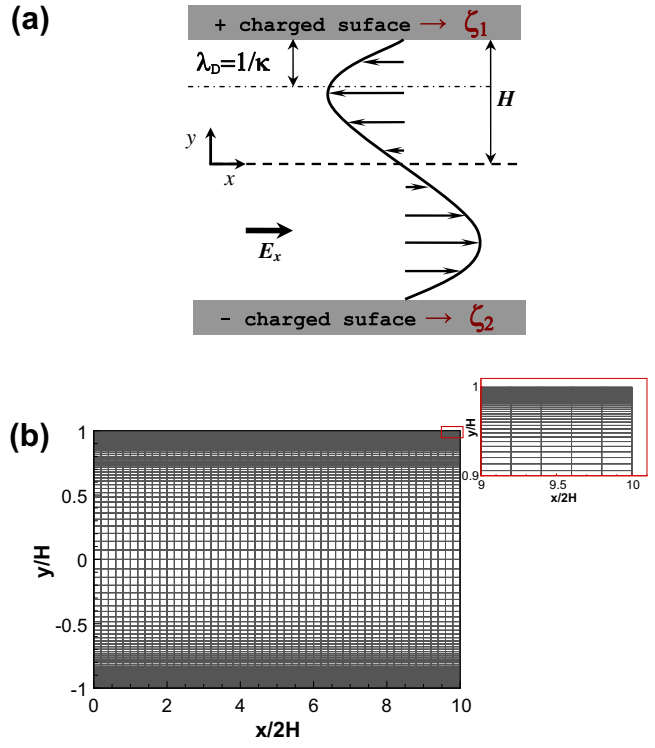

Fig. 1. Schematic representation of the (a) channel geometry and (b) computational mesh (mesh M_3). The axes are not to scale.

Table 1
Details of the channel meshes used in the code verification.

	NC	$\Delta x_{min}/H$	$\Delta y_{min}/H$
M_1	1800	0.2	8.0×10^{-4}
M_2	3600	0.2	4.0×10^{-4}
M_3	7200	0.2	2.0×10^{-4}

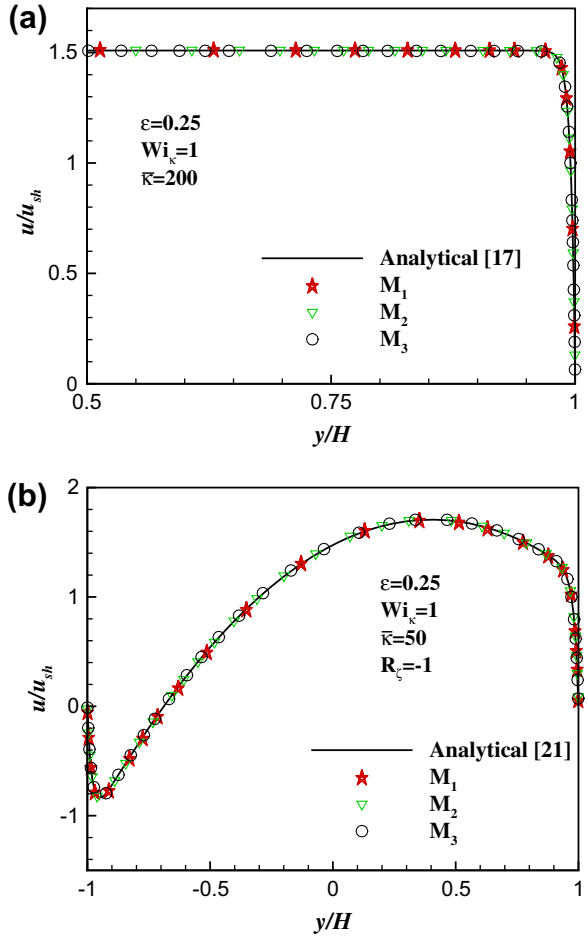

Fig. 2. Comparison between the numerical results with the PB formulation and analytical results of dimensionless velocity profiles: (a) symmetric zeta potential for pure EOF ($\Gamma = 0$, [17]); (b) asymmetric zeta potential for favorable pressure gradient ($\Gamma = -2$, [21]).

$\bar{\kappa} = 200$ and $\Gamma = 0$ (pure EOF). As observed, the analytical and numerical results collapse, showing excellent accuracy, even for a thin EDL ($\bar{\kappa} = 200$). For asymmetric flow ($R_\zeta = -1$, corresponding to anti-symmetric BC), with $\varepsilon = 0.25$, $\beta = 0$, $Wi_\kappa = 1$, $\bar{\kappa} = 50$ and in the presence of a favorable pressure gradient (with $\Gamma = -2$), the comparison between the analytical and numerical data is again excellent, as shown in Fig. 2b. These results show that the degree of refinement near the wall of mesh M_2 is sufficient to obtain accurate results, when using the PB formulation, even for very small EDL thickness.

The accuracy tests of the different implementations of electro-osmosis (the PNP formulation, and the approximations PB and PBDH) were carried out by means of a comparison between the numerical and analytical results for the velocity and ionic concentration profiles for pure electro-osmotic flow of a PTT fluid with a solvent viscosity, $\beta \neq 0$ (the analytical solution for this case is presented in Appendix A). The link between the parameters used

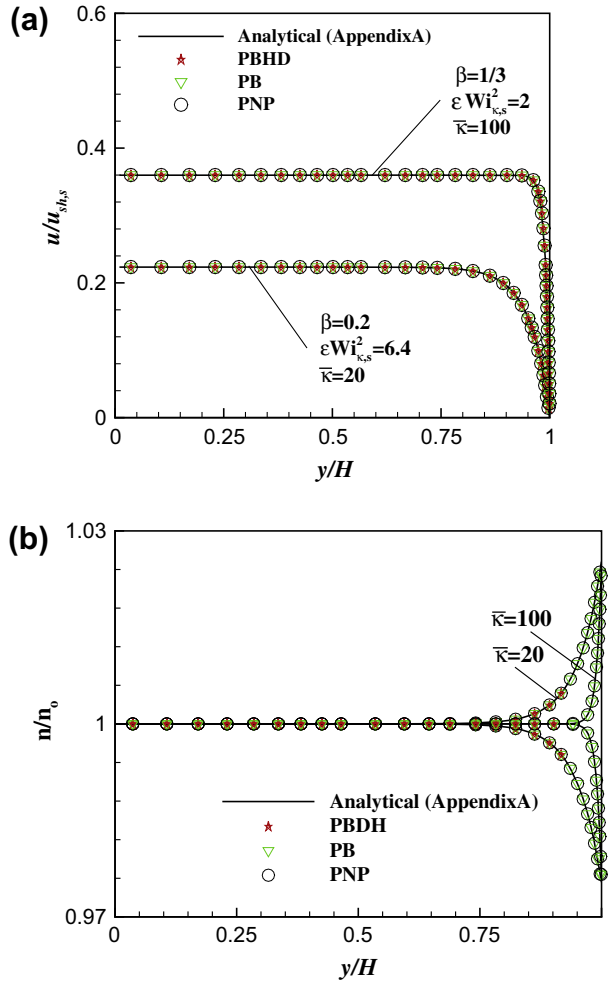

Fig. 3. Comparison between the numerical and analytical results (see Apendix A) of dimensionless (a) velocity and (b) concentration profiles, using the three formulations. Results obtained with mesh M_3.

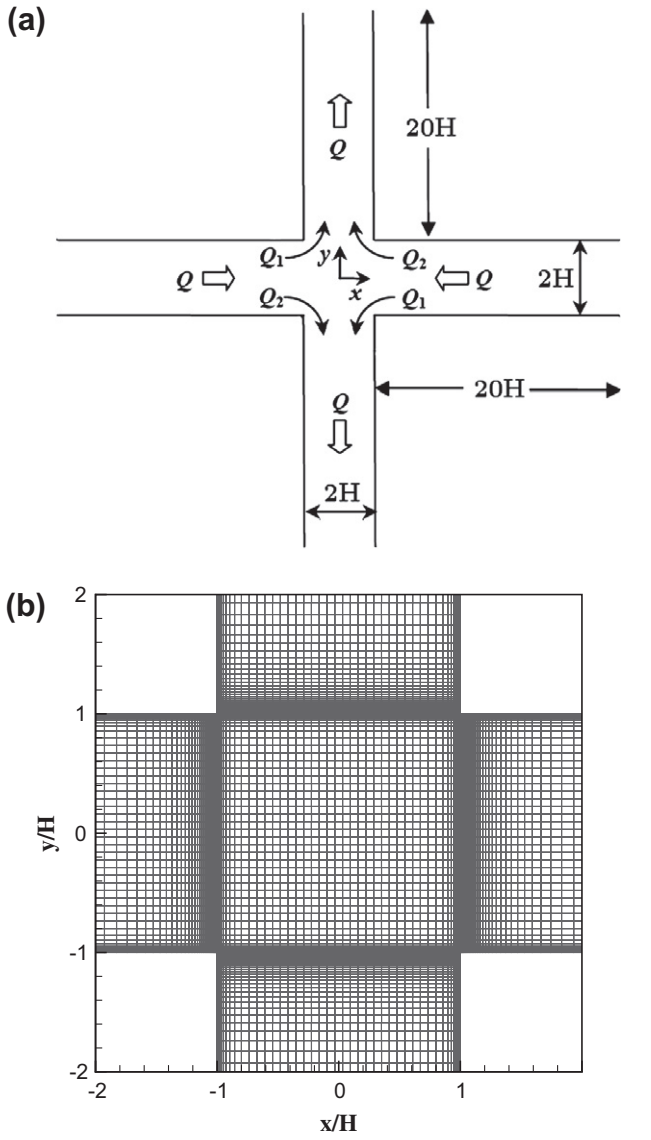

Fig. 4. Schematic representation of the (a) cross-slot geometry and (b) computational mesh M_{CS2}.

in the Poisson–Nernst–Planck model and the simplified PB and PBDH formulations is attained via the EDL thickness, by using the Debye–Hückel parameter, which is here defined as $\kappa^2 = 2\alpha\delta = 2\frac{ez}{k_BT}\frac{n_0 ez}{\epsilon}$. We consider a symmetric unitary electrolyte, that is, $z^+ = -z^- = z = 1$, a plane channel height of $H = 10^{-5}$ m, $T = 293$ K, $e = 1.60 \times 10^{-19}$ C, $\epsilon = 7 \times 10^{-10}$ F/m, $N_A = 6.02 \times 10^{23}$ mol^{-1}, $k_B = 1.38 \times 10^{-23}$ J/K, $\rho = 10^3$ kg/m^3, $\eta = 10^{-3}$ Pa s and the wall zeta potential $\zeta_1 = -25$ mV. For these conditions the non-dimensional reference zeta potential is $\alpha\zeta_1 = 0.99 \sim 1$, for which it is valid the link between the PB and the PBDH approximations to the PNP equations. Throughout this work the ratio of the microchannel to Debye layer thicknesses was kept in the range of $\bar{\kappa} = 5$—200, meaning that EDLs from the two channel walls do not overlap each other, which is typical of microscale electro-osmotic flows. When using the Poisson–Nernst–Planck formulation, the value of $\bar{\kappa} = 5$—200 is achieved by fixing the bulk ionic concentration, to be $C_o \sim 2 \times 10^{-8}$—$4 \times 10^{-5}$ M, respectively (note that $C_o = n_o/N_A$). This also means that we will work in the dilute regime, where the solute ions follow a Boltzmann distribution in the diffusion layer, according to the classical electrostatics theory. If the ionic concentration is high, the molecular interactions invalidate the Boltzmann distribution assumption. In our simulations, the typical Reynolds number is on the order of 10^{-3} and the Schmidt number is 10^3 (by setting the ionic diffusion coefficients to be $D^+ = D^- = D = 10^{-9}$ m^2/s), and, hence, the Péclet number ($Pe \equiv ScRe \equiv UH/D$) is fairly small (of the order of $Pe \sim 1$), suggesting that the contribution of hydrodynamic convection to the ionic concentration distributions is not very significant. Since the major difference between the Poisson–Nernst–Planck equations and the PB approximation lies in the capability of the former to incorporate the hydrodynamic effects on ion distribution, for the conditions considered in this case study, both formulations will give similar ionic concentration distributions.

The good agreement between the numerical predictions by all formulations and the analytical solution under the PBDH assumptions can be observed in Fig. 3a. The test cases are all within the adequate range of $\beta^3 \varepsilon Wi^2_{\kappa,s} \leqslant 2/27$ (see Appendix A) for which the analytical solution is valid. Excellent agreement is also observed for the ionic concentration distributions, as shown in Fig. 3b, which is independent of fluid rheology under fully developed flow conditions. The plotted numerical data for the ionic concentration distribution obtained with the PB and PBDH approximations were obtained from Eq. (15), while for the PNP version, $n^{\pm}$ was obtained directly from the numerical simulations of Eq. (14).

4.2. Cross-slot flow results

Further studies were undertaken in a more complex flow, usually described as cross-slot geometry (see Fig. 4), using the PB and PNP formulations. In this example, we are particularly interested in investigating the possible appearance of purely-elastic instabilities in purely EOF, as observed recently in a three-dimensional cross-slot microchannel flow by Arratia et al. [40], under pressure gradient forcing. Poole et al. [41] simulated the two-dimensional cross-slot flow of an UCM fluid under creeping-flow conditions, and were able to capture qualitatively the onset of a bistable steady asymmetric flow above a first critical Deborah number (De) followed by a later transition to a time dependent flow at higher De, in agreement with the experimental findings of Arratia et al. [40]. Poole et al. [42] later considered the three-dimensional nature of a real microfluidic cross slot flow and investigated in detail the effect of the aspect ratio of the geometry, by varying the depth of the cross slot from low values (quasi-Hele Shaw flow) up to very large values (quasi-two dimensional flow). Later, Poole et al. [43] incorporated the effect of solvent viscosity ($\beta \neq 0$ in the Oldroyd-B) and finite extensibility ($\varepsilon \neq 0$ in the sPTT model), presenting $\beta - Re - De$ and $\varepsilon - Re - De$ maps of flow pattern types and showing the existence of a narrow region of conditions where steady asymmetric flow can emerge, identifying also the limiting De for the onset of time-dependent flow. The effect of finite extensibility was also studied by Rocha et al. [44], using FENE-type models. Afonso et al. [45] presented a numerical study of the creeping flow of an UCM fluid in a three-dimensional cross-slot geometry with six arms and studied the influence of the different types of extensional flow that are generated near the stagnation point. The authors found that the uniaxial extension flow configuration is prone to the onset of steady flow asymmetries and only at higher Deborah numbers unsteady flow would emerge, while in the biaxial extension flow configuration the flow was always symmetric prior to the transition to unsteady flow.

In this work we extend the previous investigations to a new forcing mechanism by considering the effect of the electric field on the appearance of the flow instabilities. The cross-slot geometry is shown schematically in Fig. 4 together with the representation of mesh M_{CS2} used in this work. The total number of cells (NC) and the minimum cell spacing (Δx_{min} and Δy_{min}) of the two cross-slot meshes used in this work are presented in Table 2. The minimum size near the walls of the refined mesh M_{CS2} is half of the corresponding size of mesh M_2 of the accuracy tests (identical to that of mesh M_3). All branches have the same width ($2H$) and the inlet and outlet branches have lengths of twenty channel widths ($L/(2H) = 20$). For mesh M_{CS2}, the boundaries of the central square are also very refined, as can be observed in Fig. 4b, with both minimum cell spacings equal: $\Delta x_{min}/H = \Delta y_{min}/H = 2.0 \times 10^{-4}$. All the calculations were carried out at a vanishing Reynolds number, $Re = \rho UH/\eta \sim 10^{-3}$. Here, and as described in Section 4.1, the bulk ionic concentration was changed to obtain the values of $\bar{\kappa} = 5$—100, and the Péclet number was fixed at $Pe \sim 1$. To quantify the effect of the fluid elasticity, the Weissenberg number is used and defined as $Wi_\kappa = \lambda U\kappa$ (or based on the channel half-width, $Wi_H = \lambda U/H$). At the inlets the corresponding fully-developed velocity and stress profiles are imposed [17]. The cross-slot outlet channels are sufficiently long to avoid any effect of the outflow boundary condition upon the flow in the central region. No-slip conditions are imposed at all channel walls. For the potential at the walls, we assume $\partial\phi/\partial n_{|wall} = 0, \psi = \zeta_1$ and for the ionic concentration $n^{\pm}_{|wall} = n_o \exp\left(\mp \frac{ez}{k_B T}\zeta_1\right)$.

As already described, we are particularly interested in investigating the effect of the electric field in the possible appearance of asymmetries in the cross-slot flow, and in the interplay between the shear and extensional types of flow. To this purpose the simulations were undertaken with formulations PNP and PB for pure EOF conditions ($\Gamma = 0$), i.e., with null pressure difference between inlets and outlets ($p_{in} = p_{out}$), and this was achieved by fixing the desired flow rate and determining the required external electric potential difference ($\Delta\phi$) which provides $p_{in} = p_{out}$. Note that although the inlet and outlet pressures are equal, this does not mean that the pressure is constant everywhere, as observed in Fig. 5, for pure EOF of Newtonian fluids. Naturally, the flow rate in the cross-slot will be lower than would otherwise be observed in straight channel flow with the same EO forcing and channel length. The external electric potential difference necessary to impose simultaneously the same flow rate and $p_{in} = p_{out}$ depends on the dimensionless EDL width (cf. Fig. 5a), increasing for thicker Debye layers (or lower $\bar{\kappa}$). The corresponding pressure field variation along the centerline of the inlet and outlet channels is also higher for higher EDL thickness, as observed in Fig. 5b.

The effect of the EDL size on the EOF is also very important in the characterization of the flow type in the central region of the cross-slot geometry, and this is clear in Fig. 6, where the

Table 2
Details of the cross-slot meshes.

	NC	$\Delta x_{min}/H$	$\Delta y_{min}/H$
M_{CS1}	12,801	4.0×10^{-4}	4.0×10^{-4}
M_{CS2}	51,204	2.0×10^{-4}	2.0×10^{-4}

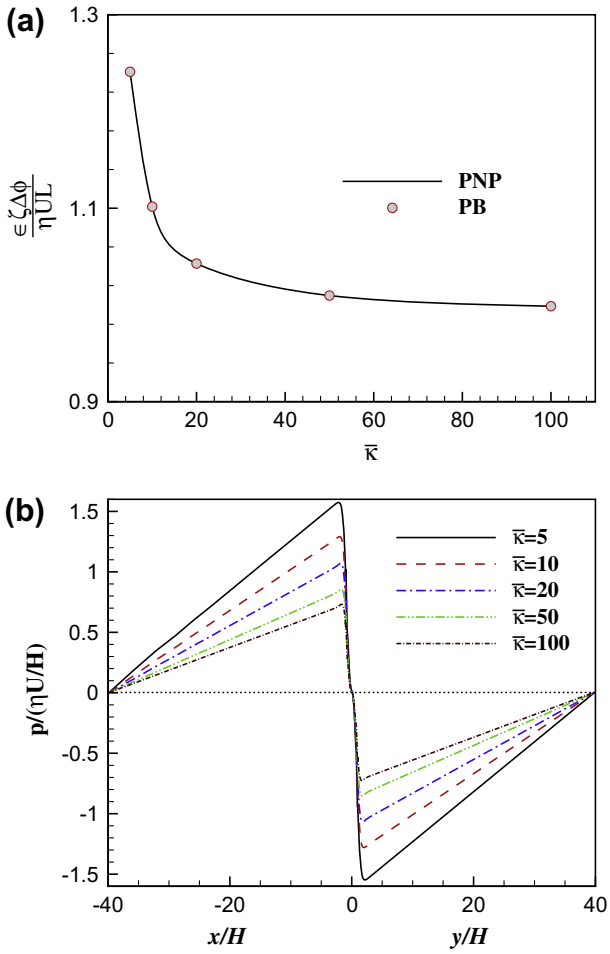

Fig. 5. (a) Imposed external electric potential ($\Delta\phi$) in dimensionless form and (b) corresponding dimensionless pressure variation along the central line of the inlet and outlet channels for pure EOF of a Newtonian fluid.

streamlines are superimposed on contour plots of the flow type parameter for pure EOF of a Newtonian fluid. The flow type parameter, ξ, is defined as [46]:

$$\xi = \frac{|\mathbf{D}| - |\boldsymbol{\Omega}|}{|\mathbf{D}| + |\boldsymbol{\Omega}|} \tag{28}$$

where $|\mathbf{D}|$ and $|\boldsymbol{\Omega}|$ represent the magnitudes of the rate of deformation and vorticity tensors, respectively

$$\mathbf{D} = \frac{1}{2}[\nabla\mathbf{u} + (\nabla\mathbf{u})^{\mathrm{T}}], \quad \boldsymbol{\Omega} = \frac{1}{2}[\nabla\mathbf{u} - (\nabla\mathbf{u})^{\mathrm{T}}], \tag{29}$$

which can be calculated as

$$|\mathbf{D}| = \sqrt{\frac{1}{2}(\mathbf{D} : \mathbf{D}^{\mathrm{T}})} = \sqrt{\frac{1}{2}\sum_i\sum_j D_{ij}^2} \tag{30}$$
$$|\boldsymbol{\Omega}| = \sqrt{\frac{1}{2}(\boldsymbol{\Omega} : \boldsymbol{\Omega}^{\mathrm{T}})} = \sqrt{\frac{1}{2}\sum_i\sum_j \Omega_{ij}^2}.$$

The flow type parameter varies from −1, which corresponds to solid-like rotation, up to 1, for pure extensional flow. Pure shear flow is characterized by $\xi = 0$. For wider EDL ($\bar{\kappa} \to 5$, cf. Fig. 6), the region of shear-dominant flow is larger, and extends from the channel walls to the central square region. Decreasing the EDL width ($\bar{\kappa} \to 100$ in Fig. 6), the shear-dominated flow is limited to the thinner region near the walls and near the corners of the central square region.

The relation between the flow type (extensional or shear dominated flow) and the type of elastic instabilities in the cross-slot (steady symmetric to steady asymmetric or directly to unstable asymmetric flow) was previously studied by several authors for pressure-driven flows [45,47,48]. Becherer et al. [47] studied analytically the effect of the boundary conditions at the inflow boundaries of the central region of the cross-slot flow geometry, arguing that the first instability observed in the cross-slot geometry [40,44] corresponds to a transition from an elongational-dominated to a shear-dominated velocity field, whereas the second transition is that of a shear dominated flow with curved streamlines. The two

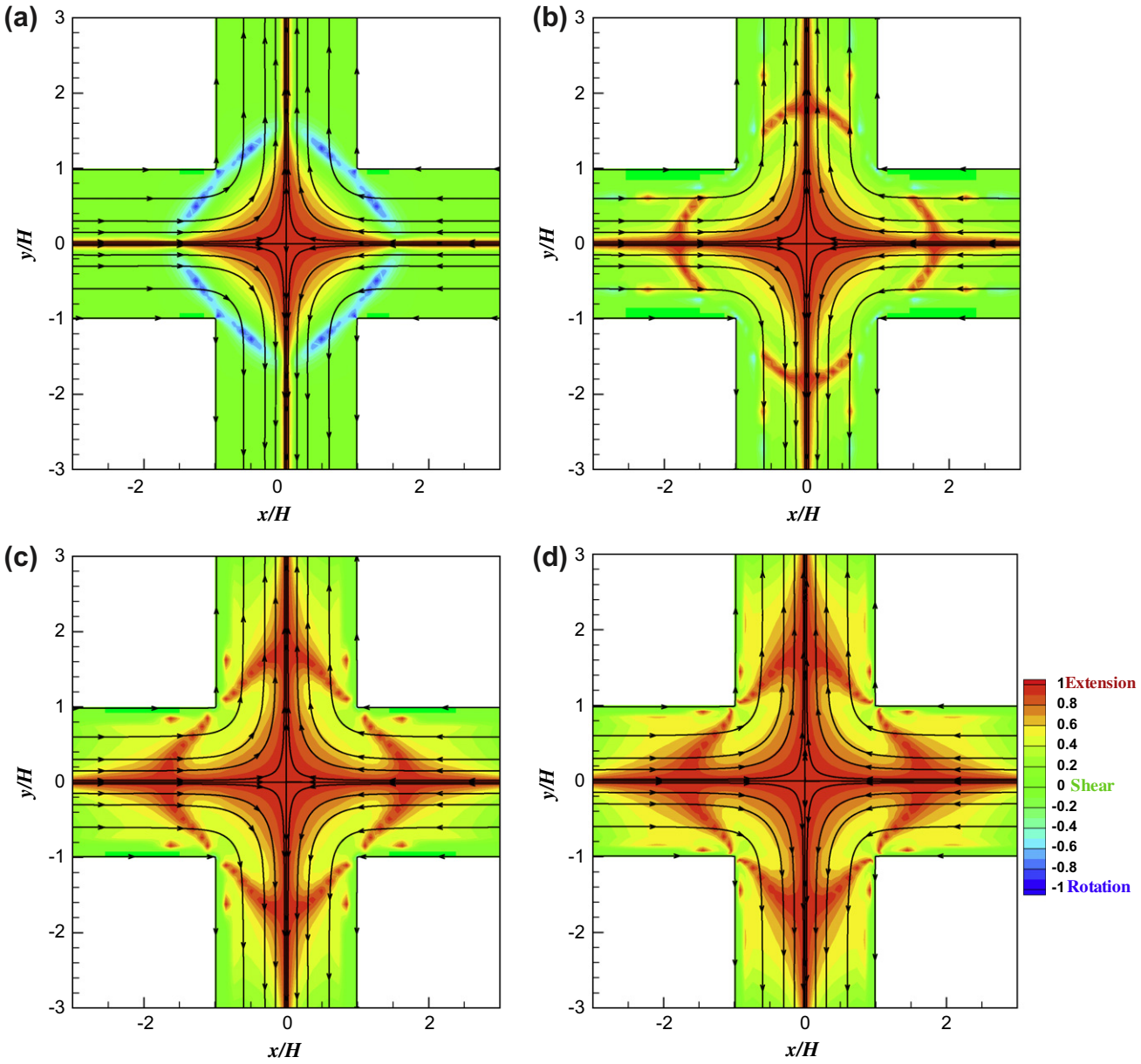

Fig. 6. Streamlines superimposed with the flow type ξ contours for Newtonian pure EOF at (a) $\bar{\kappa} = 5$, (b) $\bar{\kappa} = 20$, (c) $\bar{\kappa} = 50$ and (d) $\bar{\kappa} = 100$. The PNP formulation was used in these simulations (the results obtained with the PB approximation are similar, since $Pe \sim 1$ and dilute regime was considered).

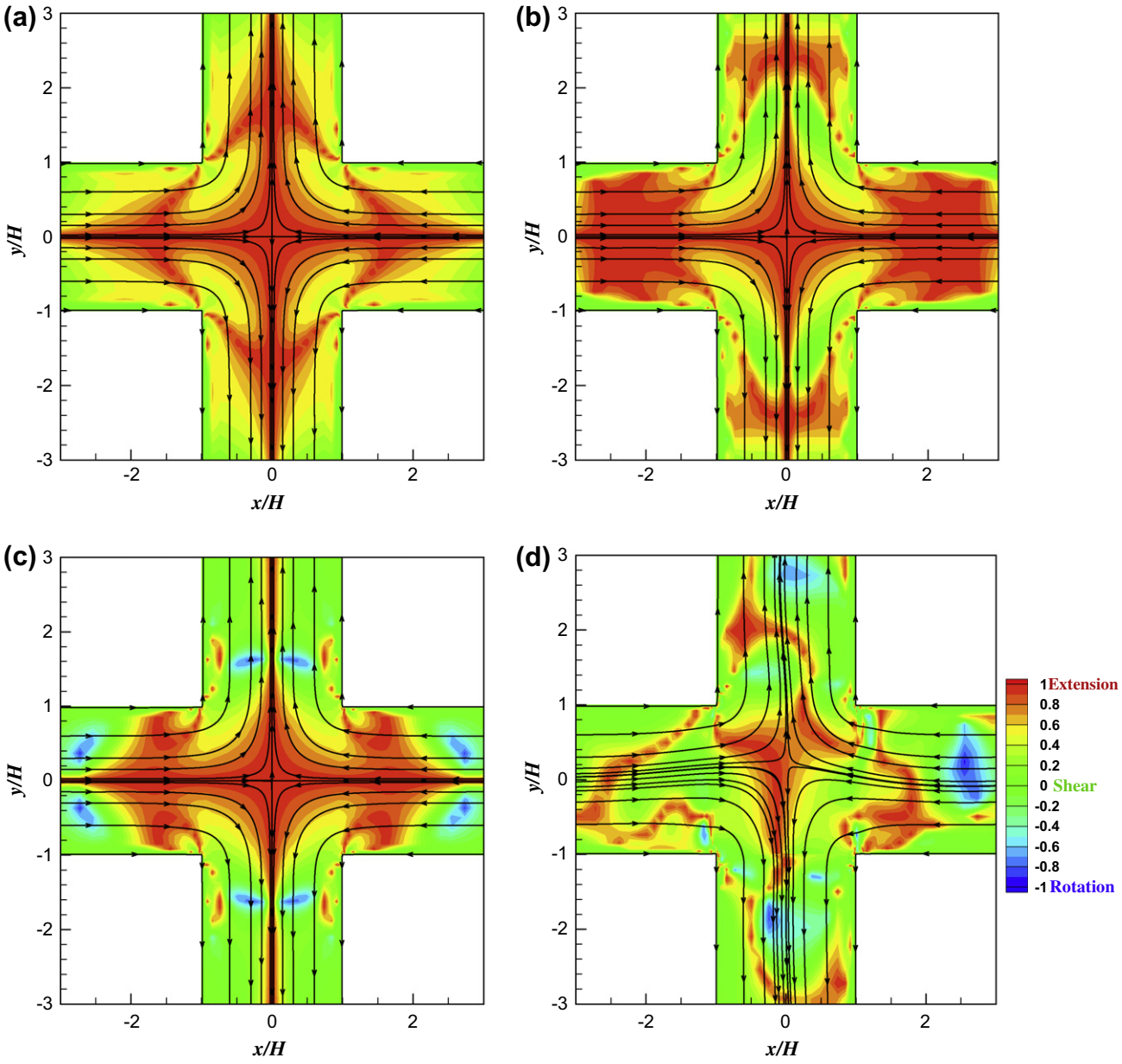

Fig. 7. Streamlines superimposed with the flow type ξ contours for UCM pure EOF and $\bar{\kappa} = 100$ at (a) $Wi_\kappa = Wi_H = 0$, (b) $Wi_\kappa \approx 2$ or $Wi_H \approx 0.02$, (c) $Wi_\kappa \approx 4$ or $Wi_H \approx 0.04$ and (d) $Wi_\kappa \approx 5$ or $Wi_H \approx 0.05$. The PNP formulation was used in these simulations (the results obtained with the PB approximation are similar, since $Pe \sim 1$ and dilute regime was considered).

flow arrangements for the 3D cross-flow simulations of Afonso et al. [45], allowed the variation of the amount of stretch and compression near the stagnation point, providing further informations on the flow instability mechanisms in extensionally dominated flows with an interior stagnation point. Specifically for the flow arrangement with four inlets and two outlets, describing a uniaxial extensional flow, the authors showed that the transition from a steady symmetric to a steady asymmetric flow was accompanied by a flow type transition, from an extensionally dominated flow to a situation where shear effects become dominant. This interplay was also discussed in the numerical work of Afonso et al. [48] performed in mixing-and-separating cells, where the two approach flows are not orthogonal as in the cross-slot flow, and consequently the shear flow becomes more important in the stagnation point region. In contrast, in the cross-slot geometry the flow is basically purely extensional, except in the vicinity of the channel walls.

For pure EOF of viscoelastic fluids, here represented by a UCM model, additional simulations were performed with both the PNP and PB formulations for several EDL widths (i.e., varying $\bar{\kappa}$). Fig. 7 presents streamlines superimposed over the flow type contour maps for increasing Weissenberg numbers, showing that for a thin EDL ($\bar{\kappa} = 100$), the flow becomes unsteady and asymmetric above a critical Weissenberg number ($Wi_\kappa \approx 5$, or $Wi_H \approx 0.05$). The onset of the unsteady asymmetric flow is accompanied by the appearance of vortex structures near the re-entrant corners of the central region of the cross-slot. This direct transition from steady symmetric to unsteady asymmetric flow was also observed in pressure-driven cross-slot flow when inertial effects are important [40,44] or for the 3D case with a biaxial extensional flow configuration [45]. In the present work, this behavior was observed independently of the corresponding EDL widths. For wider EDL (cf. $\bar{\kappa} = 20$, in Fig. 8), the increase of elasticity also leads to a direct transition from

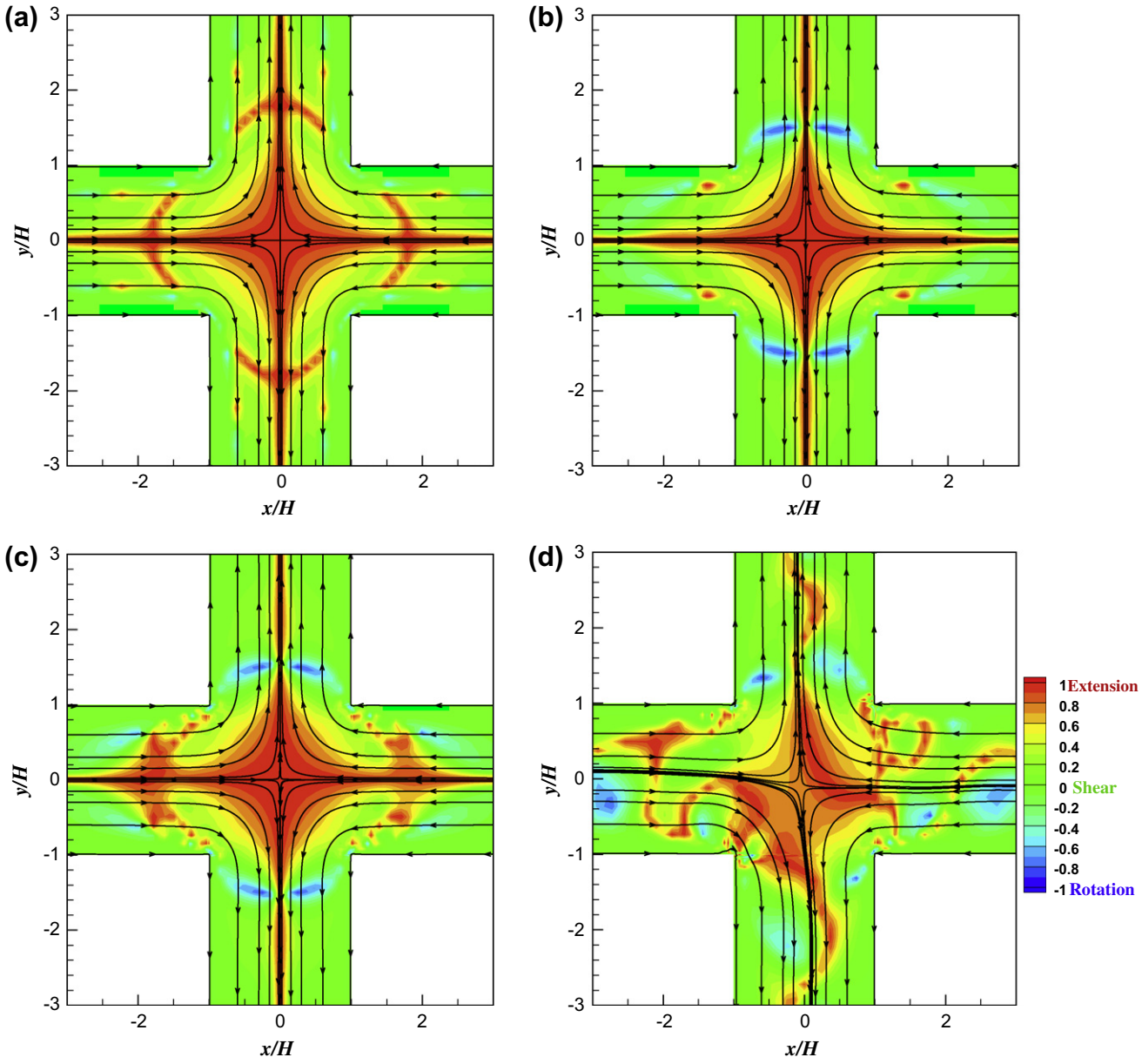

Fig. 8. Streamlines superimposed with the flow type ξ contours for UCM pure EOF and $\bar{\kappa} = 20$ at (a) $Wi_\kappa = Wi_H = 0$, (b) $Wi_\kappa \approx 2$ or $Wi_H \approx 0.1$, (c) $Wi_\kappa \approx 4$ or $Wi_H \approx 0.2$ and (d) $Wi_\kappa \approx 4.7$ or $Wi_H \approx 0.235$. The PNP formulation was used in these simulations (the results obtained with the PB approximation are similar, since $Pe \sim 1$ and dilute regime was considered).

steady symmetric to unsteady asymmetric flow, although at a different critical Weissenberg number ($Wi_\kappa \approx 4.7$, or $Wi_H \approx 0.235$).

Finally, the stability maps (Wi vs. $\bar{\kappa}$) for pure EO flow of an UCM fluid are presented in Fig. 9, for both the PNP and PB formulations and for the different Weissenberg number definitions. As expected, due to the steady behavior of the flow for $Wi < Wi_{crit}$ and since the EDL do not overlap at the center of the channels, the differences between the PNP and PB formulations are indistinguishable for small EDL sizes. Even for wider EDL, when some overlapping of the electric layers could be observed, the differences in the critical Weissenberg number are very small, within 4.4% for $\bar{\kappa} \geqslant 5$. For Weissenberg numbers above Wi_{crit}, the flow becomes unsteady, with the formation of vortical structures in the central square. In this situation, and above the critical conditions, the correct time and space distributions of ion concentrations, $n^{\pm}$, will be of major importance on the flow behavior, with the results obtained with the PNP and the PB approximation requiring further detailed studies, especially when used in combination with highly accurate time integration schemes, a task that will be undertaken in the future.

From Fig. 9 it is clear that the critical Weissenberg number, $Wi_{\kappa,crit}$, is almost constant for higher values of $\bar{\kappa}$, and detailed numerical results show that the critical region is located near the corners of the central region of the cross-slot. We can relate these instabilities with the dimensionless criterion proposed by McKinley et al. [49], based on the curvature of the flow and the tensile stress acting on the streamlines, i.e., suggesting that this transition is triggered by shear flow near the wall/corner rather than by the extension at the center. The authors expressed this criterion for the onset of elastic instability in the following dimensionless form:

$$\sqrt{\frac{\lambda u}{\Re}\frac{\tau_{11}}{\eta\dot{\gamma}}} \geqslant M_{crit} \tag{31}$$

where λ is the relaxation time of the fluid, u the local streamwise fluid velocity, $\Re$ the local radius of curvature of the streamline,

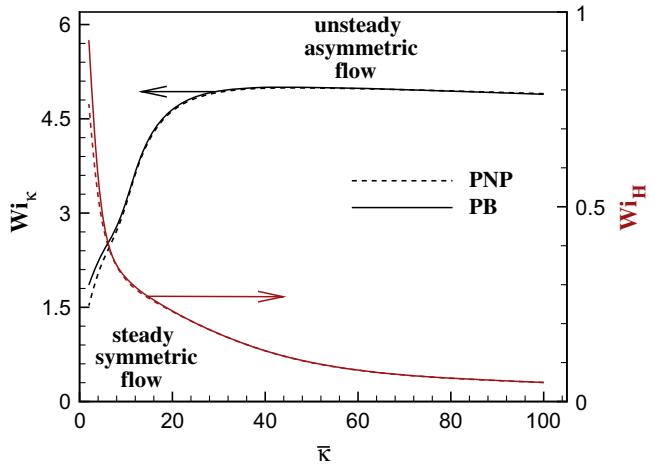

Fig. 9. Stability maps for pure EOF of an UCM fluid. Comparison between the PNP and PB formulations.

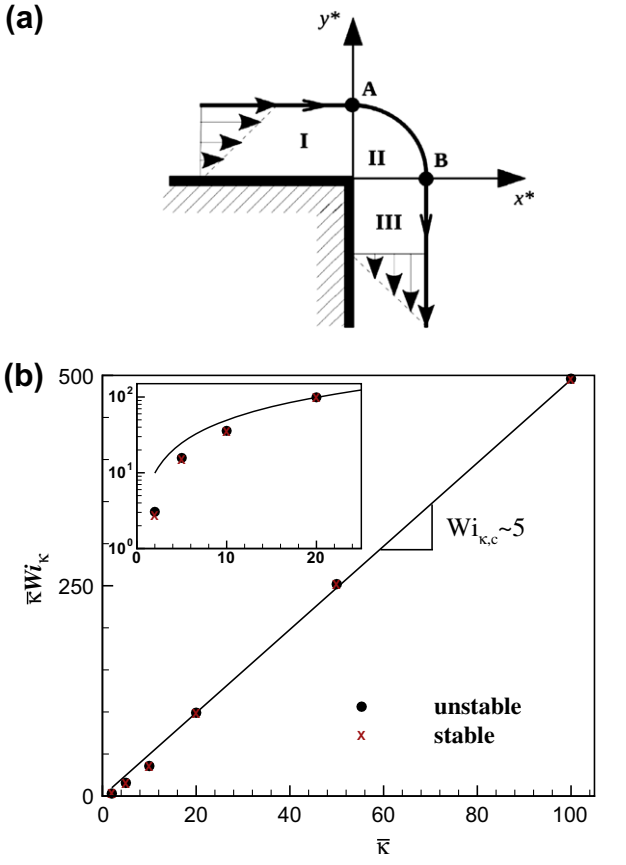

Fig. 10. (a) Illustration of the ideal flow near the reentrant corners; (b) curve $Wi_\kappa\bar{\kappa}$ vs. $\bar{\kappa}$ and dimensionless criterion for the onset of a purely elastic flow instability [49]. The fitting of the numerical data leads to $Wi_{\kappa,c} \approx 5$ or $M_{crit} \approx 7$.

τ_{11} the local tensile stress in the flow direction, η the shear viscosity of the fluid and $\dot{\gamma}$ is the local shear rate. Near the walls the flow is shear dominated, and the local tensile stress in the flow direction can be approximated as,

$$\tau_{11} = 2\lambda\eta_p\dot{\gamma}^2 \tag{32}$$

and Eq. (31) can be thought as a combination of a local Deborah number based on the streamline curvature ($\lambda u/\Re$) and a local Weissenberg number ($\lambda\dot{\gamma}$), given as

$$\sqrt{WiDe} = \sqrt{\frac{\lambda u}{\Re}\lambda\dot{\gamma}} \geqslant \frac{M_{crit}}{\sqrt{2}} \tag{33}$$

Fig. 10a presents an illustration of the ideal flow near the reentrant corners for large $\bar{\kappa}$. If we make the assumption that the velocity profile near the wall (zones I and III represented in Fig. 10a is pure shear flow, and since between points A and B there is pure rotation ($\dot{\gamma} \approx 0$) and consequently the tensile stress will decay, then the critical points will be located near $x^* = 0 (y^* > 0)$, i.e., in the vicinity of point A. In this region we can assume a linear variation of the velocity profile within the Debye layer, leading to

$$u \sim u_{sh}\frac{y^*}{\lambda_D} = u_{sh}\kappa y^*; \quad \dot{\gamma} \sim u_{sh}\kappa \tag{34}$$

and in this critical region we also estimate that the characteristic radius of curvature of the streamlines follows a linear relation with the EDL width,

$$\Re(y^*) \sim y^* \tag{35}$$

Finally, substituting Eqs. (34) and (35) into the stability criterion (i.e. Eq. (33)) leads to:

$$M_{crit} \approx \sqrt{2}Wi_{\kappa,c} \tag{36}$$

From the inspection of the slope of the curve $Wi_\kappa\bar{\kappa}$ vs. $\bar{\kappa}$ presented on Fig. 10, we can estimate that for these simulations $M_{crit} \approx \sqrt{2}Wi_{\kappa,c} \approx 7$, for low EDL thickness ($\bar{\kappa} \geqslant 20$). This value is also in agreement to those proposed to other kind of flows by McKinley et al. [49].

5. Conclusions

In this work we present a finite volume method that can be used to solve the coupled governing equations for electro-osmotic flows of viscoelastic fluids, namely the continuity equation, the momentum equation with a body force due to the applied electrical potential field and the constitutive equations for viscoelastic fluids. Three different physical models describing the electric charge density distribution were implemented, which depend on the desired level of approximation. In the first implementation, the Poisson–Nernst–Planck equations were incorporated into the viscoelastic code and the electric charge density distribution required to quantify the electric forcing in the momentum equation is calculated from the most fundamental governing equations. The second implementation is an approximation in which a stable Boltzmann distribution of ions is assumed to occur in the electric double layer, represented by the Poisson–Boltzmann equations. Finally, the so-called Debye–Hückel approximation of the PB model was also implemented denoting the Poisson–Boltzmann–Debye–Hückel model, which is valid for cases with a small ratio of electrical to thermal energies. To describe the rheological behavior of viscoelastic fluids we use the UCM and sPTT [18] models. The implementation of the numerical method was assessed through comparison with existing analytical solutions for the flow in a two-dimensional microchannel under symmetric and asymmetric boundary conditions for the zeta potential at the walls, and the comparison between the analytical and numerical results showed excellent agreement, even for small EDL thickness.

In this work we further extend our previous investigations on pressure driven cross-slot flow by considering the effect of the electric field on the appearance of electro-elastic flow instabilities. For the UCM fluid the flow becomes asymmetric but time-dependent above a critical Weissenberg number, for all EDL widths studied. This contrasts to events in pressure driven creeping flow where there is first a transition from steady symmetric to steady asymmetric flow at $Wi_H = 0.309$ and, subsequently, a second transition from steady asymmetric flow to unsteady asymmetric flow at higher Wi_H [41]. In EO-driven creeping flow, the critical Weissenberg

number for the direct transition from steady symmetric to unsteady asymmetric flow decreases with the decrease of the thickness of the EDL, ranging from $Wi_H \approx 0.235$ to $Wi_H \approx 0.05$ for $\bar{\kappa} = 20$ and $\bar{\kappa} = 100$ respectively. The onset of the unsteady asymmetric flow is accompanied by the appearance of vortex structures near the re-entrant corners of the central region of the cross-slot. The differences between the results for pressure driven and EO driven flows are related with the flow type within the central region and in particular to the shear flow which was found to be less stabilizing in the case of EOF. This suggests that this transition is triggered by shear flow near the wall/corner rather by the extensional flow at the center. Indeed, using the dimensionless criterion for the onset of instabilities proposed by McKinley et al. [49], which is based on the curvature of the flow and the tensile stress along the streamlines, we estimate that for these simulations $M_{crit} \approx 7$, for low EDL thickness ($\bar{\kappa} \geqslant 20$), a value which is in agreement to those proposed for other pressure-driven flows [49].

As a secundary result of this investigation, Appendix A presents the full analytical solution for fully developed electro-osmosis driven flow of polymer solutions described by the sPTT or FENE-P models with a Newtonian solvent, which is used for validation purposes. This analytical solution was obtained assuming a thin electric double layer.

Acknowledgments

The authors acknowledge funding from FEDER and Fundação para a Ciência e a Tecnologia (FCT), Portugal, through Projects PTDC/EQU-FTT/70727/2006 and PTDC/EQU-FTT/113811/2009. A.M. Afonso would also like to thank FCT for financial support through the scholarship SFRH/BPD/75436/2010.

Appendix A. Analytical solution for fully-developed pure electro-osmosis flow in a straight channel for the PTT and FENE-P fluid models with Newtonian solvent viscosity

For fully developed channel flow of viscoelastic fluids driven by electro-osmosis, the momentum equation – Eq. (2) – reduces to

$$\frac{d\tau_{xy}}{dy} = -\rho_e E_x - \eta_s \frac{d^2u}{dy^2} \tag{A.1}$$

where u is the streamwise velocity and y is the transverse coordinate. In this flow the Poisson–Boltzmann distribution is valid and additionally we invoke the Debye–Hückel approximation (see [17] for justifications). Eq. (12) can be solved subjected to the boundary conditions at the walls, $\psi(H) = \psi(-H) = \zeta_1$, to give,

$$\psi = \zeta_1 \frac{\cosh(\kappa y)}{\cosh(\kappa H)} \tag{A.2}$$

valid for $-H \leqslant y \leqslant H$. The net charge density distribution, Eq. (17), in conjunction with Eq. (A.2) reduces to

$$\rho_e = -\epsilon\zeta_1\kappa^2 \frac{\cosh(\kappa y)}{\cosh(\kappa H)} \tag{A.3}$$

which is a positive quantity for a wall charged negatively ($\zeta_1 < 0$). Eq. (A.1) can now be integrated, noting that $\tau_{xy\|y=0} = 0$ (centerline symmetry condition), to yield

$$\tau_{xy} = \epsilon\zeta_1 E_x \kappa \frac{\sinh(\kappa y)}{\cosh(\kappa H)} - \eta_s \frac{du}{dy} \tag{A.4}$$

For the same fully-developed flow conditions, the non-zero extra-stress components for the PTT model are defined as,

$$f(\tau_{kk})\tau_{xx} = 2\lambda \frac{du}{dy}\tau_{xy} \tag{A.5}$$

$$f(\tau_{kk})\tau_{xy} = \eta_p \frac{du}{dy} \tag{A.6}$$

where $\tau_{kk} = \tau_{xx}$, because $\tau_{yy} = \tau_{zz} = 0$ [17,21], and $\frac{du}{dy}$ is the velocity gradient. Then, upon division of Eq. (A.5) by Eq. (A.6) the specific function $f(\tau_{xx})$ cancels out, and the following relation between the normal and shear stresses is obtained,

$$\tau_{xx} = 2\frac{\lambda}{\eta_p}\tau_{xy}^2 \tag{A.7}$$

Function $f(\tau_{kk})$ is the linear form of Eq. (5) written in terms of the stress tensor, i.e., $f(\tau_{kk}) = 1 + \lambda\varepsilon\tau_{kk}/\eta_p$, with τ_{kk} representing the trace of the stress tensor.

Using these relations, an explicit expression for the normal stress component can be obtained,

$$\tau_{xx} = 2\frac{\lambda}{\eta_p}\left(\epsilon\zeta_1 E_x \kappa \frac{\sinh(\kappa y)}{\cosh(\kappa H)} - \eta_s \frac{du}{dy}\right)^2 \tag{A.8}$$

Note that Eq. (A.8) is consistent with the required boundary condition at the centerline, i.e. $\tau_{xx\|y=0} = 0$. From Eqs. (A.6) and (A.4) we obtain,

$$\left(1 + 2\frac{\varepsilon\lambda^2}{\eta_p^2}\tau_{xy}^2\right)\tau_{xy} = \eta_p \frac{du}{dy} = \frac{\eta_p}{\eta_s}\left(-\tau_{xy} + \epsilon\zeta_1 E_x \kappa \frac{\sinh(\kappa y)}{\cosh(\kappa H)}\right) \tag{A.9}$$

After rearranging the various terms in Eq. (A.9) we arrive at the standard form of a cubic equation for τ_{xy}:

$$\tau_{xy}^3 + \frac{\eta_p^2}{2\varepsilon\lambda^2}\left(\frac{\eta_s + \eta_p}{\eta_s}\right)\tau_{xy} - \frac{\eta_p^2}{2\varepsilon\lambda^2}\left(\epsilon\zeta_1 E_x \kappa \frac{\eta_p}{\eta_s}\frac{\sinh(\kappa y)}{\cosh(\kappa H)}\right) = 0 \tag{A.10}$$

which can be written in compact form as

$$\tau_{xy}^3 + p\tau_{xy} = q \tag{A.11}$$

with

$$p = \frac{\eta_p^2}{2\beta\varepsilon\lambda^2}$$

$$q = -\frac{\eta_p^3}{2\varepsilon\lambda^2} u_{sh,s}\kappa \frac{\sinh(\kappa y)}{\cosh(\kappa H)} \tag{A.12}$$

where $\beta = \frac{\eta_s}{\eta_s+\eta_p}$, $\frac{\eta_p}{\eta_s} = \frac{1-\beta}{\beta}$ and $u_{sh,s} = -\frac{\epsilon\zeta_1 E_x}{\eta_s}$. The real solution of this cubic equation is

$$\tau_{xy} = 2\sqrt{\frac{\eta_p^2}{6\beta\varepsilon\lambda^2}} \times \sinh\left\{\frac{1}{3}\operatorname{arc\,sinh}\left[-\frac{\eta_p^3}{4\varepsilon\lambda^2}u_{sh,s}\kappa\frac{\sinh(\kappa y)}{\cosh(\kappa H)}\left(\frac{\eta_p^2}{6\beta\varepsilon\lambda^2}\right)^{-\frac{3}{2}}\right]\right\} \tag{A.13}$$

Eq. (A.9) can be explicity written with respect to the velocity gradient as:

$$\frac{du}{dy} = -\frac{2}{\eta_s}\sqrt{\frac{\eta_p^2}{6\beta\varepsilon\lambda^2}} \times \sinh\left\{\frac{1}{3}\operatorname{arc\,sinh}\left[-\frac{\eta_p^3}{4\varepsilon\lambda^2}u_{sh,s}\kappa\frac{\sinh(\kappa y)}{\cosh(\kappa H)}\left(\frac{\eta_p^2}{6\beta\varepsilon\lambda^2}\right)^{-\frac{3}{2}}\right]\right\} - u_{sh,s}\kappa\frac{\sinh(\kappa y)}{\cosh(\kappa H)} \tag{A.14}$$

In order to integrate Eq. (A.14), we assume the following variable transformation and approximation, $\varphi = \sinh(\kappa y) \approx \frac{1}{2}\exp(\kappa y)$. This

approximation is usually accurate as in many practical applications the finite electric double layer is very small, about 1 to 3 orders of magnitude smaller than the width of the microfluidic channel. Defining $\frac{du}{dy} \simeq \frac{du}{d\varphi}.\kappa\varphi$ and $\varphi_{cos} = \cosh(\kappa H)$, Eq. (A.14) can be approximated as:

$$\frac{du}{d\varphi} = -\frac{u_{sh,s}}{\varphi_{cos}} - \frac{2}{\eta_s \kappa \varphi}\sqrt{\frac{\eta_p^2}{6\beta\varepsilon\lambda^2}} \times \sinh\left\{\frac{1}{3}\operatorname{arc\,sinh}\left[-u_{sh,s}\kappa\frac{\eta_p^3}{4\varepsilon\lambda^2}\frac{\varphi}{\varphi_{cos}}\left(\frac{\eta_p^2}{6\beta\varepsilon\lambda^2}\right)^{-\frac{3}{2}}\right]\right\} \quad (A.15)$$

Eq. (A.15) can now be integrated subject to the no-slip boundary condition at the wall ($u_{\|y=H} = 0$ or $u_{\|\varphi=\sinh(\kappa H)=\varphi_H} = 0$) and the resulting velocity profile is

$$u(\varphi) = -u_{sh,s}\left(\frac{\varphi}{\varphi_{cos}} - \frac{\varphi_H}{\varphi_{cos}}\right) + u_{sh,s}(1-\beta) \times \frac{\varphi}{\varphi_{cos}}\sum_{n=0}^{\infty}\frac{\left(\frac{1}{3}\right)_n\left(\frac{1}{2}\right)_n\left(\frac{2}{3}\right)_n}{\left(\frac{3}{2}\right)_n\left(\frac{3}{2}\right)_n}\frac{\left[-\frac{27}{2}\beta^3\varepsilon Wi_{\kappa,s}^2\left(\frac{\varphi}{\varphi_{cos}}\right)^2\right]^n}{n!} - u_{sh,s}(1-\beta)\frac{\varphi_H}{\varphi_{cos}}\sum_{n=0}^{\infty}\frac{\left(\frac{1}{3}\right)_n\left(\frac{1}{2}\right)_n\left(\frac{2}{3}\right)_n}{\left(\frac{3}{2}\right)_n\left(\frac{3}{2}\right)_n} \times \frac{\left[-\frac{27}{2}\beta^3\varepsilon Wi_{\kappa,s}^2\left(\frac{\varphi_H}{\varphi_{cos}}\right)^2\right]^n}{n!} \quad (A.16)$$

which can be written in compact form as

$$\frac{u(\varphi)}{u_{sh,s}} = \frac{\varphi_H}{\varphi_{cos}} - \frac{\varphi}{\varphi_{cos}} + (1-\beta)\left[\frac{\varphi}{\varphi_{cos}}\Omega(\varphi) - \frac{\varphi_H}{\varphi_{cos}}\Omega(\varphi_H)\right] \quad (A.17)$$

with $\Omega(\varphi)$ representing the following hypergeometric function

$$\Omega(\varphi) = \sum_{n=0}^{\infty}\frac{\left(\frac{1}{3}\right)_n\left(\frac{1}{2}\right)_n\left(\frac{2}{3}\right)_n}{\left(\frac{3}{2}\right)_n\left(\frac{3}{2}\right)_n}\frac{\left[-\frac{27}{2}\beta^3\varepsilon Wi_{\kappa,s}^2\left(\frac{\varphi}{\varphi_{cos}}\right)^2\right]^n}{n!} \quad (A.18)$$

The symbol $(a)_n$ (Pochhammer symbol) is a rising factorial defined as $(a)_n = a(a+1)\ldots(a+n-1)$. This specific hypergeometric function has a radius of convergence of 1, meaning that it only converges for $\left|-\frac{27}{2}\beta^3\varepsilon Wi_{\kappa,s}^2\left(\frac{\varphi}{\varphi_{cos}}\right)^2\right| \leqslant 1$. This limits this analytical solution to the condition $\beta^3\varepsilon Wi_{\kappa,s}^2 \leqslant 2/27$. For $\left|-\frac{27}{2}\beta^3\varepsilon Wi_{\kappa,s}^2\left(\frac{\varphi}{\varphi_{cos}}\right)^2\right| > 1$ the hypergeometric function can be calculated by analytic continuation, but not using series (A.18).

In these equations the following normalizations were introduced: $\bar{y} = y/H$, $\bar{\kappa} = \kappa H$ and $Wi_{\kappa,s} = \frac{\lambda u_{sh,s}}{\lambda_D} = \lambda\kappa u_{sh,s}$ is the Weissenberg number based on the EDL thickness and on the solvent Helmholtz–Smoluchowski electro-osmotic velocity.

Given that this solution is valid for thin EDL, we can use again the approximation $\varphi = \sinh(\kappa y) \approx \frac{1}{2}\exp(\kappa y)$, to arrive at a more compact velocity profile,

$$\frac{u(\bar{y})}{u_{sh,s}} = \tanh(\bar{\kappa}) - \frac{\sinh(\bar{\kappa}\bar{y})}{\cosh(\bar{\kappa})} + (1-\beta)\left[\frac{\sinh(\bar{\kappa}\bar{y})}{\cosh(\bar{\kappa})}\Omega(\bar{y}) - \tanh(\bar{\kappa})\Omega(1)\right] \quad (A.19)$$

with

$$\Omega(\bar{y}) = \sum_{n=0}^{\infty}\frac{\left(\frac{1}{3}\right)_n\left(\frac{1}{2}\right)_n\left(\frac{2}{3}\right)_n}{\left(\frac{3}{2}\right)_n\left(\frac{3}{2}\right)_n}\frac{\left[-\frac{27}{2}\beta^3\varepsilon Wi_{\kappa,s}^2\left(\frac{\sinh(\bar{\kappa}\bar{y})}{\cosh(\bar{\kappa})}\right)^2\right]^n}{n!} \quad (A.20)$$

As stated before, the EDL size in many practical applications is very small ($\bar{\kappa} \gtrsim 10$), and in these circumstances $\cosh(\bar{\kappa}) \gg 1$ and $\overline{D} = \tanh(\bar{\kappa}) \approx 1$, so the above equation can be further simplified to,

$$\frac{u(\bar{y})}{u_{sh,s}} = 1 - \frac{\sinh(\bar{\kappa}\bar{y})}{\cosh(\bar{\kappa})} + (1-\beta)\left[\frac{\sinh(\bar{\kappa}\bar{y})}{\cosh(\bar{\kappa})}\Omega(\bar{y}) - \Omega(1)\right] \quad (A.21)$$

For steady fully developed channel flow, the PTT and the FENE-P models exhibit similar behavior as found by Oliveira [50]. In these circumstances there is an exact equivalence between the PTT and the FENE-P models in the sense of a parameter to parameter match, as explained in detail in Cruz et al. [51], with the following change of variables,

$$\begin{aligned} f(\tau_{xx}) &\to \left(\frac{b+2}{b+5}\right)Z(\tau_{xx}) \\ \lambda &\to \lambda\left(\frac{b+2}{b+5}\right) \\ \varepsilon &\to \frac{1}{b+5} \\ \eta_p &\to \eta_p \end{aligned} \quad (A.22)$$

Then, providing these substitutions are made in the non-dimensional velocity profiles for the PTT model – Eqs. (A.19)–(A.21), the results of this Appendix remain valid for the FENE-P fluid.

References

[1] H. Bruus, Theoretical Microfluidics, Oxford Master Series in Condensed Matter Physics, Oxford University Press, Oxford, UK, 2008.
[2] F.F. Reuss, Sur un nouvel effet de l'électricité galvanique, Mém. Soc. Impériale Nat. Moscou 2 (1809) 327–337.
[3] H. Helmholtz, Studien über electrische Grenzschichten, Ann. Phys. 243 (1879) 337–382.
[4] M. von Smoluchowski, Versuch einer mathematischen Theorie der Koagulationskinetik kolloider Lösungen, Z. Phys. Chem. 92 (1917) 129–135.
[5] G. Gouy, Sur la Constitution de la Charge Électrique la Surface d'un Électrolyte, J. Physiol. 9 (1910) 457–468.
[6] D.L. Chapman, A contribution to the theory of electrocapillarity, Philos. Mag. Ser. 6 25 (148) (1913) 475–481.
[7] P. Debye, E. Hückel, Zur Theorie der Elektrolyte: II. Grensgesetz für die elektrische Leitfähigkeit, Phys. Z. 24 (1923) 305–325.
[8] D. Burgreen, F.R. Nakache, Electrokinetic flow in ultrafine capillary slits, J. Phys. Chem. 68 (1964) 1084–1091.
[9] C.L. Rice, R. Whitehead, Electrokinetic flow in a narrow cylindrical capillary, J. Phys. Chem. 69 (1964) 4017–4024.
[10] S. Arulanandam, D. Li, Liquid transport in rectangular microchannels by electroosmotic pumping, Colloids Surf. A. 161 (2000) 29–102.
[11] P. Dutta, A. Beskok, Analytical solution of combined electroosmotic/pressure driven flows in two-dimensional straight channels: finite Debye layer effects, Anal. Chem. 73 (2001) 1979–1986.
[12] G. Karniadakis, A. Beskok, N. Aluru, Microflows and nanoflows, in: Fundamentals and Simulation, Interdisciplinary Applied Mathematics Series, vol. 29, Spinger Verlag, 2005.
[13] S. Das, S. Chakraborty, Analytical solutions for velocity, temperature and concentration distribution in electroosmotic microchannel flows of a non-Newtonian bio-fluid, Anal. Chim. Acta 559 (2006) 15–24.
[14] H.M. Park, W. M Lee, Helmholtz–Smoluchowski velocity for viscoelastic electroosmotic flows, J. Colloid Interface Sci. 317 (2008) 631–636.
[15] C.L.A. Berli, M.L. Olivares, Electrokinetic flow of non-Newtonian fluids in microchannels, J. Colloid Interface Sci. 320 (2008) 582–589.
[16] C. Zhao, E. Zholkovskij, J.H. Masliyah, C. Yang, Analysis of electroosmotic flow of power-law fluids in a slit microchannel, J. Colloid Interface Sci. 326 (2008) 503–510.
[17] A.M. Afonso, M.A. Alves, F.T. Pinho, Analytical solution of mixed electro-osmotic/pressure driven viscoelastic fluids in microchannels, J. Non-Newt. Fluid Mech. 159 (2009) 50–63.
[18] N. Phan-Thien, R.I. Tanner, New constitutive equation derived from network theory, J. Non-Newt. Fluid Mech. 2 (1977) 353–365.
[19] N. Phan-Thien, A non-linear network viscoelastic model, J. Rheol. 22 (1978) 259–283.
[20] R.B. Bird, R.C. Armstrong, O. Hassager, Dynamics of polymeric liquids, Fluid Mechanics, second ed., vol. 1, Wiley, New York, 1987.
[21] A.M. Afonso, M.A. Alves, F.T. Pinho, Electro-osmotic flows of viscoelastic fluids in microchannels under asymmetric zeta potential, J. Eng. Math. 71 (2011) 15–30.

[22] J.J. Sousa, A.M. Afonso, F.T. Pinho, M.A. Alves, Effect of the skimming-layer on electro-osmotic – Poiseuille flows of viscoelastic fluids, Microfluid. Nanofluid. 10 (2011) 107–122.
[23] C. Yang, D. Li, Analysis of electrokinetic effects on the liquid flow in rectangular microchannels, J. Colloids Surfaces 143 (1998) 339–353.
[24] N.A. Patankar, H.H. Hu, Numerical simulation of electroosmotic flow, Anal. Chem. 70 (1998) 1870–1881.
[25] S.V. Ermakov, S.C. Jacobson, J.M. Ramsey, Computer simulation of electrokinetic transport in micro fabricated channel structures, Anal. Chem. 70 (1998) 4494–4504.
[26] F. Bianchi, R. Ferrigno, H.H. Girault, Finite element simulation of an electroosmotic-driven flow division at a T-junction of microscale dimension, Anal. Chem. 72 (2000) 1987–1993.
[27] P. Dutta, A. Beskok, T.C. Warburton, Numerical simulations of mixed electroosmotic/pressure driven microflows, Numer. Heat Transfer – Part A 41 (2002) 131–148.
[28] P. Dutta, A. Beskok, T.C. Warburton, Electroosmotic flow control in complex microgeometries, J. Microelectromech. Syst. 11 (1) (2002) 36–44.
[29] J.Y. Lin, L.M. Fu, R.J. Yang, Numerical simulation of electrokinetic focusing in microfluidic chips, J. Micromech. Microeng. 12 (2002) 955–961.
[30] H.M. Park, W.M. Lee, Effect of viscoelasticity on the flow pattern and the volumetric flow rate in electroosmotic flows through a microchannel, Lab Chip 8 (2008) 1163–1170.
[31] G.H. Tang, X.F. Li, Y.L. He, W.Q. Tao, Electroosmotic flow of non-Newtonian fluid in microchannels, J. Non-Newt. Fluid Mech. 157 (2009) 133–137.
[32] G.H. Tang, P.X. Ye, W.Q. Tao, Pressure-driven and electroosmotic non-Newtonian flows through microporous media via lattice Boltzmann method, J. Non-Newt. Fluid Mech. 165 (2010) 1536–1542.
[33] W.B. Zimmerman, J.M. Rees, T.J. Craven, Rheometry of non-Newtonian electrokinetic flow in a microchannel T-junction, Microfluid. Nanofluid. 2 (2006) 481–492.
[34] R.M. Bryce, M.R. Freeman, Abatement of mixing in shear-free elongationally unstable viscoelastic microflows, Lab Chip 10 (2010) 1436–1441.
[35] R. Fattal, R. Kupferman, Constitutive laws of the matrix-logarithm of the conformation tensor, J. Non-Newt. Fluid Mech. 123 (2004) 281–285.
[36] A.M. Afonso, F.T. Pinho, M.A. Alves, The Kernel-conformation constitutive laws, J. Non-Newt. Fluid Mech. 167–168 (2012) 30–37.
[37] P.J. Oliveira, F.T. Pinho, G.A. Pinto, Numerical simulation of non-linear elastic flows with a general collocated finite-volume method, J. Non-Newt. Fluid Mech. 79 (1998) 1–43.
[38] M.A. Alves, P.J. Oliveira, F.T. Pinho, A convergent and universally bounded interpolation scheme for the treatment of advection, Int. J. Numer. Methods Fluids 41 (2003) 47–75.
[39] A. Afonso, P.J. Oliveira, F.T. Pinho, M.A. Alves, The log-conformation tensor approach in the finite-volume method framework, J. Non-Newt. Fluid Mech. 157 (2009) 55–65.
[40] P.E. Arratia, C.C. Thomas, J.D. Diorio, J.P. Gollub, Elastic instabilities of polymer solutions in cross-channel flow, Phys. Rev. Lett. (2006) 144502.
[41] R.J. Poole, M.A. Alves, P.J. Oliveira, Purely elastic flow asymmetries, Phys. Rev. Lett. 99 (2007) 164503.
[42] R.J. Poole, M.A. Alves, A.M. Afonso, F.T. Pinho, P.J. Oliveira, Purely-elastic instabilities in a microfluidic cross-slot geometry, AIChE 2007 Annual Meeting, Salt Lake City, Paper 94827, 2007.
[43] R.J. Poole, M.A. Alves, A.M. Afonso, F.T. Pinho, P.J. Oliveira, Purely elastic instabilities in a cross-slot flow, The Society of Rheology 79th Annual Meeting, Salt Lake City, 2007.
[44] G.N. Rocha, R.J. Poole, M.A. Alves, P.J. Oliveira, On extensibility effects in the cross-slot flow bifurcation, J. Non-Newt. Fluid Mech. 156 (2009) 58–69.
[45] A.M. Afonso, M.A. Alves, F.T. Pinho, Purely-elastic flow instabilities in a 3D six arms cross slot geometry, J. Non-Newt. Fluid Mech. 165 (2010) 743–751.
[46] J.S. Lee, R. Dylla-Spears, N.P. Teclemariam, S.J. Muller, Microfluidic four-roll mill for all flow types, Appl. Phys. Lett. 90 (2007) 074103.
[47] P. Becherer, A.N. Morozov, W. van Saarloos, Scaling of singular structures in extensional flow of dilute polymer solutions, J. Non-Newt. Fluid Mech. 153 (2008) 183–190.
[48] A.M. Afonso, M.A. Alves, R.J. Poole, P.J. Oliveira, F.T. Pinho, Viscoelastic flows in mixing-separating cells, J. Eng. Math. 71 (1) (2011) 3–13.
[49] G.H. McKinley, P. Pakdel, A. Öztekin, Rheological and geometric scaling of purely elastic flow instabilities, J. Non-Newt. Fluid Mech. 67 (1996) 19–47.
[50] P.J. Oliveira, An exact solution for tube and slit flow of a FENE-P fluid, Acta Mech. 158 (2002) 157–167.
[51] D.O.A. Cruz, F.T. Pinho, Fully-developed pipe and planar flows of multimode viscoelastic fluids, J. Non-Newt. Fluid Mech. 141 (2007) 85–98.